A hierarchically porous MOF confined $CsPbBr_3$ quantum dots: Fluorescence switching probe for detecting melamine in food samples

Highlights

In this chapter highly luminescent $CsPbBr_3$ perovskites were confined into a hierarchically porous ZIF-8 metal organic framework (HZIF-8). The resulting stable $CsPbBr_3$/HZIF-8 composite is used as an on-off-on fluorescence sensing probe for melamine detection in aqueous medium and extend its applicability for real sample analysis in milk samples.

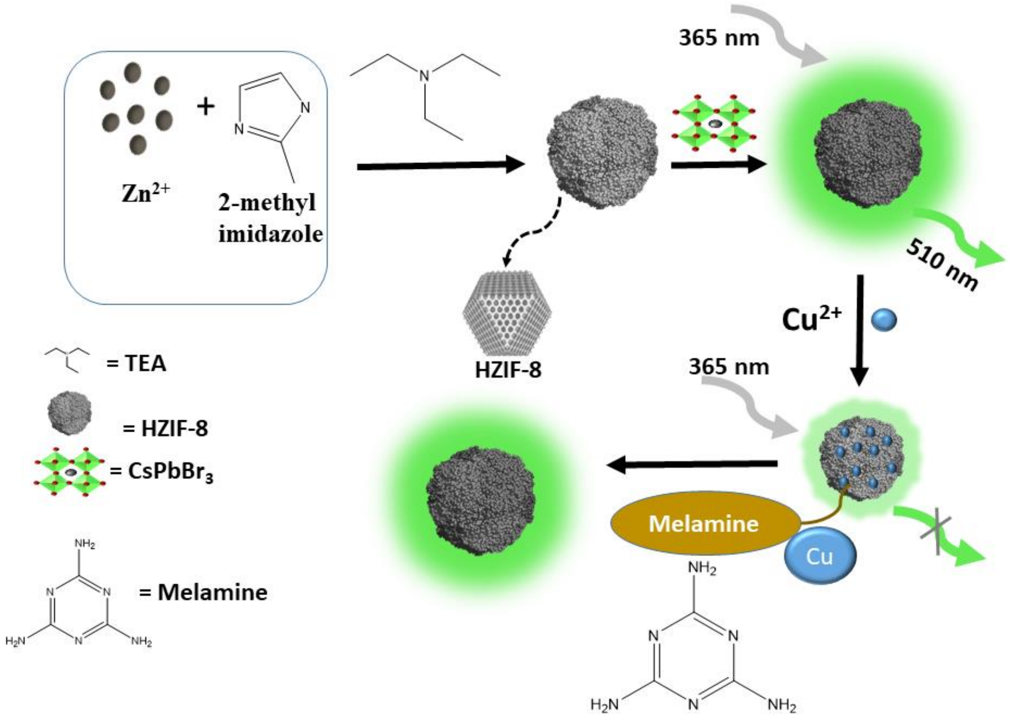

This part of the thesis is published as-

Ahmed, S., Lahkar, S., Doley, S., Mohanta, D., and Dolui, S. K. A hierarchically porous MOF confined $CsPbBr_3$ quantum dots: Fluorescence switching probe for detecting Cu (II) and melamine in food samples. *Journal of Photochemistry and Photobiology A: Chemistry*, 443:114821, 2023.

4.1. Introduction

2,4,6-triamino-1,3,5-triazine (Melamine) is a nitrogen rich organic base and an industrial raw material, generally used in the production of melamine-formaldehyde resins for plastic and paint industries, adhesives, coatings, and fire-retardant materials, etc. However, melamine has received major attention in the aspects of food safety following a crisis concerning melamine-contaminated milk in 2008 [1]. Owing to its high nitrogen content, melamine is illegally added to dairy products, and feedstuffs to enhance the protein content and thus misguided the consumers. Cyanuric acid, the hydrolysis product of melamine, has generated a less soluble melamine cyanurate complex and eventually precipitates in the renal tubules, causing further tissue injury and urinary calculus [2]. Consuming melamine-containing food over an extended period of time at levels above the safety limit (20 μM in the USA and EU, 8 μM for infant formula in China) can possibly be fatal, especially in infants and children [3]. Therefore, it is crucial to develop an efficient detection technique for traces of melamine in the food and feed industries to prevent adulteration and protect food safety. Advanced analytical techniques such as high-performance liquid chromatography (HPLC) [4], liquid chromatography-mass spectrometry (LC-MS) [5], electrochemical methods [6], colorimetry [7], surface-enhanced Raman spectroscopy [8], enzyme-linked immunosorbent assays [9], Fourier transform infrared spectroscopy (FT-IR), and fluorescence spectroscopy have been used to develop potential assays for melamine detection [1]. Amongst them, the fluorometric method provides a simple, low-cost, highly selective, and sensitive method for the successful detection of melamine.

Utilizing the ultrahigh porosity of MOF as host matrices for various luminescent guest molecules with high PLQY has been designed to produce functionalized luminescent MOF based nanocomposite [10, 11]. It has been shown that encapsulating highly luminescent $CsPbX_3$ perovskites in the MOF matrices to create host-guest composites is an easy and effective approach [12-16]. **Chapter 3** described the use of a microporous Zeolitic imidazolate framework (ZIF-8) with superior chemical stability for Pe-MOF composite synthesis. The microporous system has limited diffusion of guest molecules, thereby hierarchically porous ZIF-8 (HZIF-8) has great interest. In HZIF-8, mesopores are introduced in the ZIF-8 that results in a mixture type of both micropores and mesopores in ZIF-8 that increase the diffusion rate of reactants [12,16,17].

In an effort to widen the analytical applications of PeNCs, our present work introduces a confined synthesis of $CsPbBr_3$ PeNCs within the hierarchically porous MOF (HZIF-8) via an in situ growth method. The method uses HZIF-8 as support to grow PeQDs directly within the MOF system with uniform crystal size and highly luminescent properties. HZIF-8 was synthesized following a triethylamine-assisted method. The stability of PeNCs within the MOF is highly improved and maintains the bright PL in harsh environmental conditions (moisture, water, temperature, light, etc.). Functionalization of $CsPbBr_3$ quantum dots (QDs) with the HZIF-8 MOF host combines the advantages of both the unique and outstanding luminescence properties of perovskite nanocrystals and the ability of efficient accumulation and adsorption of target analytes by the MOF matrix enabling them to be effective sensing probe and thereby demonstrating great selectivity and sensitivity. Therefore, $CsPbBr_3$/H-ZIF8 composites were utilized as fluorescence turn-off-on sensors for the quantitative detection of melamine in food samples with a very low limit of detection (LOD) value of 2.64 nM. Here, the metal ion (Cu^{2+}) acts as a quenching agent for the green PL signal of $CsPbBr_3$/H-ZIF8 composite. Melamine as a multifunctional system can competitively adsorb Cu^{2+} from the surface of the sensing probe due to the strong interaction between melamine nitrogen and Cu and the quenched PL signal is restored and thus develops an on-off-on fluorescence sensor.

4.2 Experimental Section

4.2.1 Materials

Lead bromide ($PbBr_2$, 99.9%), Cesium bromide (CsBr, 99.9%), zinc nitrate hexahydrate ($Zn(NO_3)_2.6H_2O$, 99%) were purchased from alfa aesar. 2-methyl imidazole (HmIM), (99%, SRL chemicals), methanol (MeOH, 99.5%, SRL chemicals), N,N-dimethylformamide (DMF, 99%, Merck), toluene (C_7H_8, Merck), triethyl amine (TEA, 99%, Merck), melamine ($C_3H_6N_6$, 99%, alfa aesar). The chemicals in this work were purchased from commercial sources and used exactly as received.

4.2.2 Methods

4.2.2.1 Synthesis of HZIF-8

HZIF-8 was synthesized according to a previously used method with minor modifications [18]. In this process, 0.8 ml of $Zn(NO_3)_2·6H_2O$ solution (0.8 mmol) in deionized water was first mixed with 0.10 ml (0.70 mmol) of TEA, and then 2.3 mL of the HmIM solution was added (6.4 mmol). The final molar ratio of metal to linker was 1:8. Using deionized water, the reaction volume was filled to a total of 28 ml. After a continuous stirring of 30 min at room temperature, the white precipitates were formed which were collected using centrifugation. The obtained products were washed several times with water/ethanol mixture and dried overnight at 70 °C in a vacuum oven.

4.2.2.2 $CsPbBr_3$/HZIF-8 composite

In a typical synthesis procedure of $CsPbBr_3$/HZIF-8 composite, the HZIF-8 MOF (150 mg) was first dispersed in 10 ml DMF. Then 2 mmol of $PbBr_2$ was added into the dispersion with continuous stirring for 5 h. The $PbBr_2$@MOF powder was collected by filtering the solution. In the second step, the resulting powder was dispersed in toluene (10 ml) with stirring. Then, the CsBr/methanol solution (1.0 mmol) was quickly injected into the toluene dispersion that induces the crystallization of perovskite quantum dots and finally produced perovskite-MOF composite. The whole experiment was performed at room temperature in an ambient atmosphere. The yellowish colored precipitates were collected by filtration and washed thoroughly with methanol.

4.2.2.3 Sample preparation and fluorescence measurement

5 mg ml^{-1} $CsPbBr_3$/HZIF-8 composite solution served as the standard and sonicated for 15 min to get a homogeneous dispersion. Thereafter emission intensity was measured using the 3 ml of aqueous dispersion of composite. Various concentrations of Cu^{2+} metal ions were added into the 3 ml standard QD solution and incubating at room temperature for 5 min. At the end of the incubation time, the PL spectra of the solutions were measured at 365 nm excitation wavelength with 10 nm slit width using a 1cm^3 quartz cuvette. For the melamine assay, a 1 mM stock solution was first prepared and then diluted to various concentrations by adding to a buffer solution (pH 6.5). 100 µl volume of prepared melamine solution was then added to 3 ml of $CsPbBr_3$/H-ZIF-8 dispersion (5 mg ml^{-1}) with 600 nM Cu^{2+} and homogenized. After incubation at room temperature for 5 min, the fluorescence spectra were recorded at 365 nm excitation (excitation and emission slit of 10 nm).

4.2.2.4 Pretreatment of real samples

Milk samples were pretreated before melamine detection according to the literature [19]. 2 ml of raw milk sample was mixed with 1 mL of acetonitrile, 1 ml of trichloroacetic acid, and 5 mL of water. The mixture was ultra-sonicated for 10 min followed by centrifugation for 10 min at 4500 rpm to separate the deposit. The obtained supernatant was filtered through a 0.45 μm PTFE filter. The filtrate was adjusted to pH 7.0 and diluted with 10 mL of water to obtain the samples for further experiments.

4.2.2.3 Detection of melamine in real samples: We bought infant formula at the neighbourhood grocery store, Tezpur University. Various known concentrations (0, 45, 85 and 145 nM) of melamine were added to the pre-treated milk sample. Then 4 ml of the $CsPbBr_3$/HZIF-8+Cu^{2+} (5 mg ml^{-1} and 600 nM Cu^{2+}) sample volume was mixed with the milk samples with known concentration of melamine for FL measurements at excitation wavelength of 365 nm and recovery of melamine was calculated.

4.3 Results and discussion

The hierarchically porous MOF, HZIF-8 was synthesized by a template free simple triethylamine assisted method, in which free mesopores are generated in ZIF-8 without removing the template. The as synthesized HZIF-8 was utilized to embed the $CsPbBr_3$ (CPB) PeNCs by a surfactant free two-step approach. The $CsPbBr_3$/HZIF-8 nanohybrids were developed to create a high-performance sensing probe. All the synthesized materials were characterized with various analytical tools.

4.3.1. XRD and FTIR analysis

The highly crystalline structure of the synthesized HZIF-8 MOF powder was identified using powder X-ray diffraction (XRD), which is shown in Figure 4.1a. The diffraction peaks were located at around $2\theta = 7.60^0$, 10.57^0, 12.85^0, 14.8^0, 16.6^0, 18.12^0, 19.70^0, 24.6^0, 25.75^0, 26.78^0, 29.74^0, 30.66^0 and 32.36^0, corresponding to the (011), (002), (112), (022), (013), (222), (114), (233), (224), (134), (044), (244) and (235) planes of the ZIF-8 MOF [20]. The distinctive peaks of the PXRD pattern of HZIF-8 are in good agreement with those of the ZIF-8 pattern.

The FTIR spectrum (Figure 4.1b) of CPB@HZIF-8 preserves the specific vibrations of the MOF, indicating that the MOF matrix successfully passivated the CPB PeQDs.

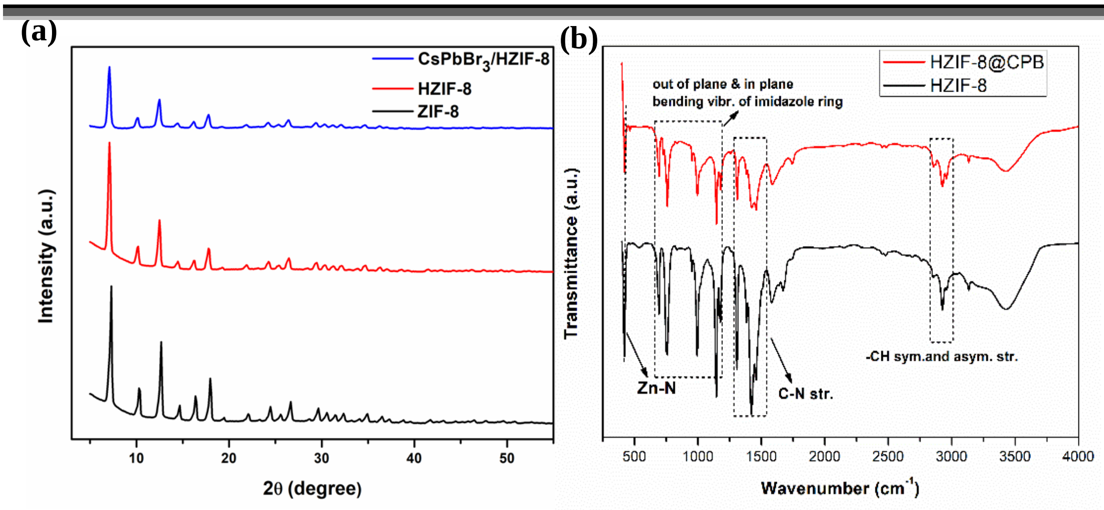

Figure 4.1: Powder XRD pattern of ZIF-8, HZIF-8 MOF, and $CsPbBr_3$/HZIF-8 (a), FTIR spectra of HZIF-8 MOF and CPB/HZIF-8 MOF composite (b).

4.3.2. EDX analysis

The occupancy of $CsPbBr_3$ in the MOF matrix can further be confirmed by the XPS and EDX analysis. EDX spectra of the composite showed the presence of Cs, Pb, and the signal of Br along with Zn and N demonstrating the successful formation of $CsPbBr_3$ in the HZIF-8 MOF matrix (Figure 4.2).

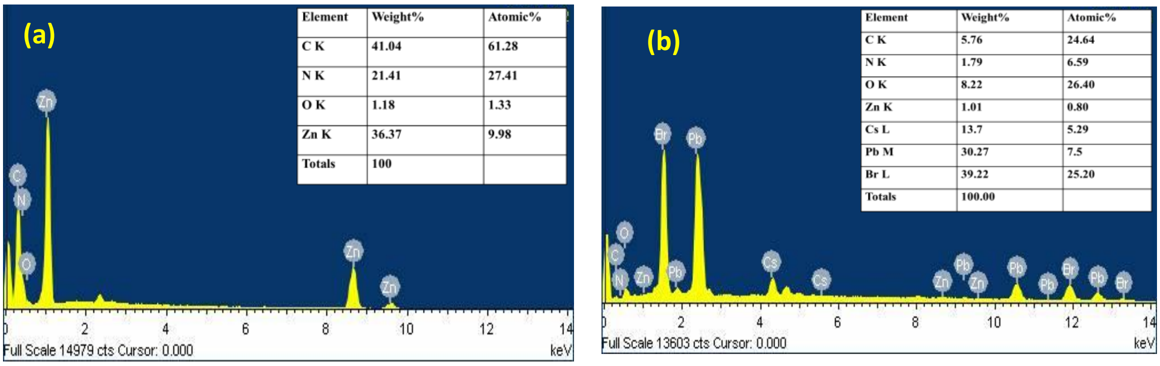

Figure 4.2: EDX spectra of HZIF-8 (a), $CsPbBr_3$/HZIF-8 (b).

4.3.3. XPS analysis

XPS analysis was carried out to determine the surface characteristics and chemical state of the $CsPbBr_3$/H-ZIF8 MOF composite. As illustrated in the survey XPS spectrum (Figure 4.3a), the presence of desired signals of Cs, Pb, and Br on the surface of the PeQD@MOF composite coupled with the C, N, and Zn^{2+} signal from the HZIF-8 matrix, clearly validate the formation of $CsPbBr_3$ nanocrystal in the MOF matrix. The XPS fine spectra displays feature peaks of Cs $3d_{5/2}$ (724.2 eV) and Cs $3d_{3/2}$ (738.2 eV), Pb $4f_{7/2}$

(138.1 eV), Pb $4f_{5/2}$ (143 eV) and Br $3d_{5/2}$ (67.9 eV), Br $3d_{3/2}$ (69.1 eV) (Figure 4.3). These values are closely matched with the previous literature reported for $CsPbBr_3$ PeQD [21]. The Zn *2p* peaks appeared at binding energies of 1022 eV and 1045.1 eV (Figure 4.4a) and were derived from Zn $2P_{3/2}$ and Zn $2P_{1/2}$ states respectively from the HZIF-8. Figure 4.4b shows the high-resolution XPS spectrum of C*1s*, which further can be deconvoluted into two peaks at 284.6 eV (C-H/ C=C) and 285.2 eV (C-N), both of which are from imidazole ring. Similarly, the N1s spectrum could be fitted into four peaks centered at 398.6 eV, 399.6 eV, 400.3 eV, and 403 eV. The peak at 398.6 eV corresponding to N-Zn coordinate bond and the peaks at 399.6 eV, 400.3 eV mainly contributed to the N-C and N-H moieties (Figure 4.4c). Higher energy N*1s* peak at 403 eV assigned to the quaternary nitrogen ion which indicates the existence of N-Pb interaction through non coordinated nitrogen from 2-methyl imidazole linker, thereby signifying a close interaction between PeQDs and the MOF matrix. The XPS analysis results strongly support the formation of the $CsPbBr_3$/HZIF-8 MOF composite.

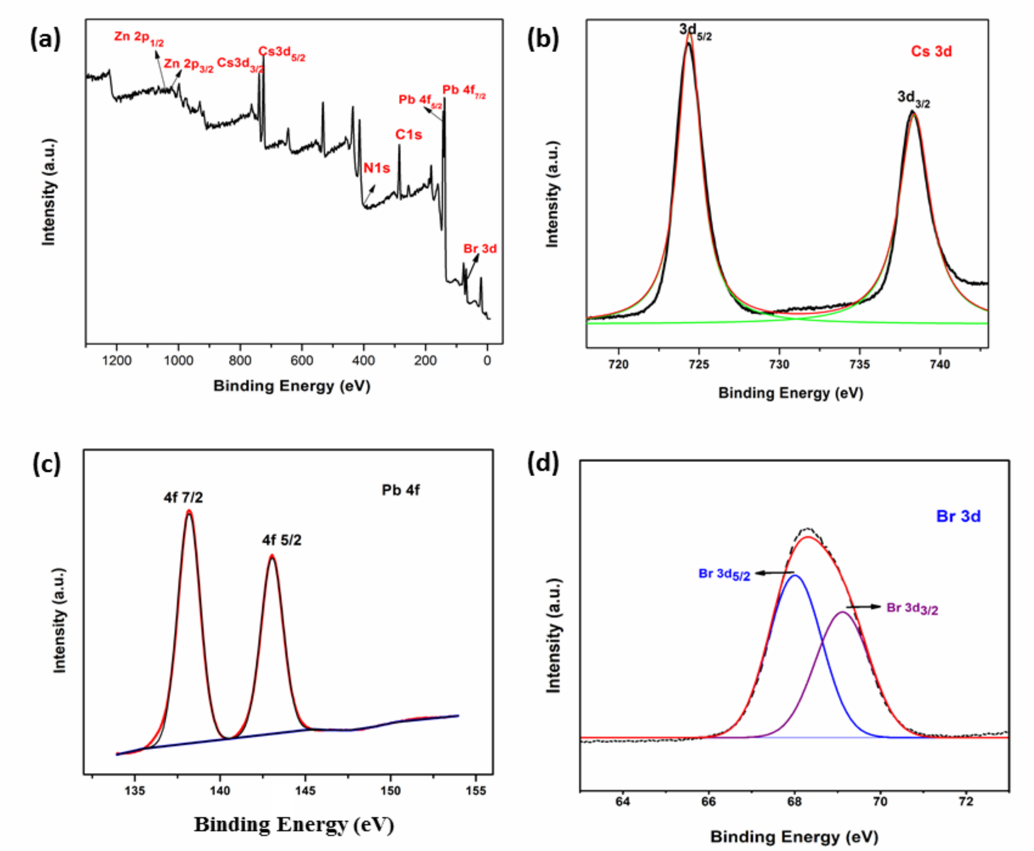

Figure 4.3: XPS survey spectrum of $CsPbBr_3$/HZIF-8 (a), High resolution XPS spectra of Cs *3d* (b), Pb *4f* (c), and Br *3d* (d).

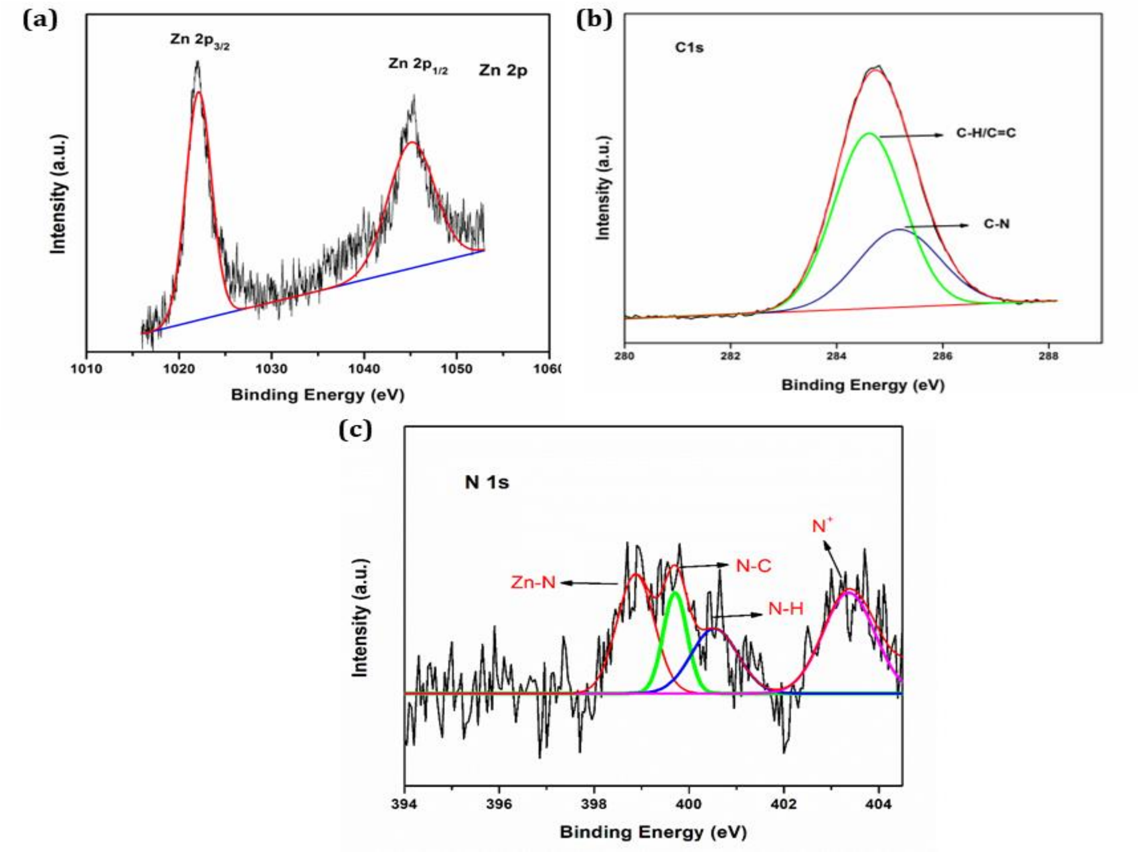

Figure 4.4: XPS fine spectra of Zn *2p* (a), C *1s* (b), and N *1s* (c).

4.3.4. Morphological analysis

SEM and TEM micrograph pictures were taken. The SEM images of pristine HZIF-8 show monodisperse bouquet-like morphology with a densely packed surface with an average size of about 70 nm (Figure 4.5a). Further, TEM images of the $CsPbBr_3$/HZIF-8 show the well-defined $CsPbBr_3$ PeNCs, are embedded by the porous MOF matrix forming a core shell type structure. A large number of $CsPbBr_3$ quantum dots (QDs) can be seen as dark circular areas without any visible particles outside the HZIF-8 MOF matrix. The high-resolution transmission electron microscopy (HR-TEM) image of the constrained $CsPbBr_3$ PeNCs in HZIF-8 MOF with clearly defined lattice spacing is shown in Figure 4.5c and Figure 4.5d, demonstrating their great crystallinity. The interplanar spacing calculated from the lattice fringes are 0.288 nm and 0.238 nm corresponding to the (200) and (211) planes of the cubic $CsPbBr_3$ respectively [13]. Based on the aforementioned results, the $CsPbBr_3$ QDs are safeguarded by the protective MOF shell that would lead to improved stability of the perovskite MOF binary composite.

Additionally, the identical diffraction peaks of $CsPbBr_3$/HZIF-8 in Figure 4.1a imply that the growth of $CsPbBr_3$ PeQDs into HZIF-8 does not compromise its crystalline integrity. Because of the small size of $CsPbBr_3$ and very high crystallinity of HZIF-8 MOF in comparison to $CsPbBr_3$, the peak intensities associated with it could be screened by the diffraction peaks of the MOF matrix and hence the XRD pattern does not exhibit any prominent peaks of $CsPbBr_3$. From the TEM images of the $CsPbBr_3$/HZIF-8 composite the average grain size of the PeQDs was found to be about 4 nm (<5 nm), much smaller than that of the MOF host. The relative intensities of the diffraction peak diminished and broadened which is likely due to the changes in electron density within the matrix with the loading of the $CsPbBr_3$ to the MOF matrix. Therefore, the framework structure of MOF is preserved in all the prepared samples. Similar results were found in other literature also [12, 13].

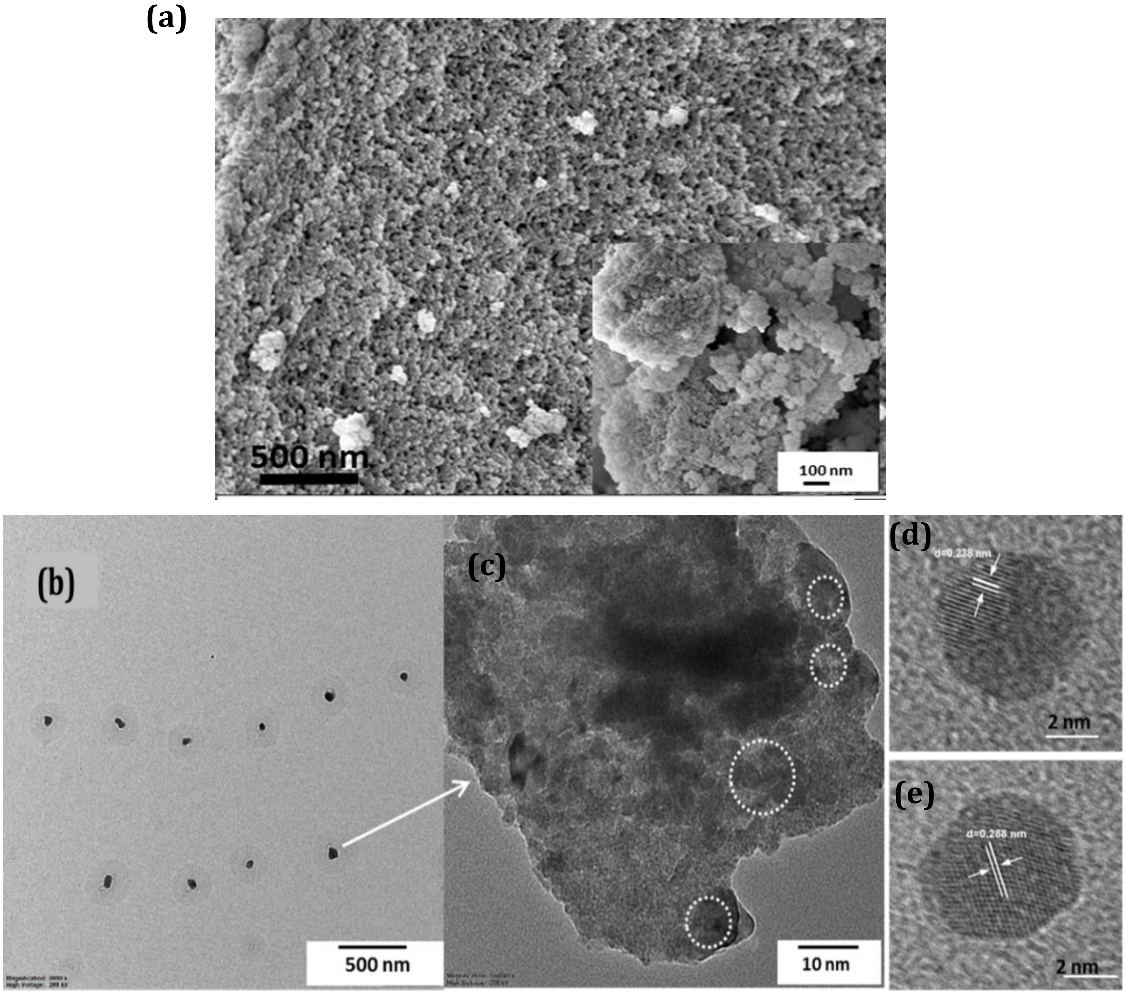

Figure 4.5: SEM image of HZIF-8, inset: close up view of the MOF (a), TEM images of $CsPbBr_3$/HZIF-8 MOF composite (b, c), and HRTEM images of enlarge view of the core of the composite/selected zone (d, e).

4.3.5. BET analysis

The hierarchical porous characteristics of HZIF-8 encompassing both meso and microporosity are confirmed by the N_2 adsorption-desorption isotherm with a prominent hysteresis loop. The pore size distribution of HZIF-8 in Figure 4.6 and Table 4.1 illustrates the mixture of type I and type IV adsorption-desorption isotherms in HZIF-8. BET (Brunauer–Emmett–Teller) surface area of the HZIF-8 is calculated to be 2065.237 m^2g^{-1}. When the nonporous PeQDs further grow in situ into the pore channels of HZIF-8, pore volume and the BET surface area of the perovskite confined MOF are significantly decreased, attributed to the successful incorporation of the PeQDs in the MOF matrix.

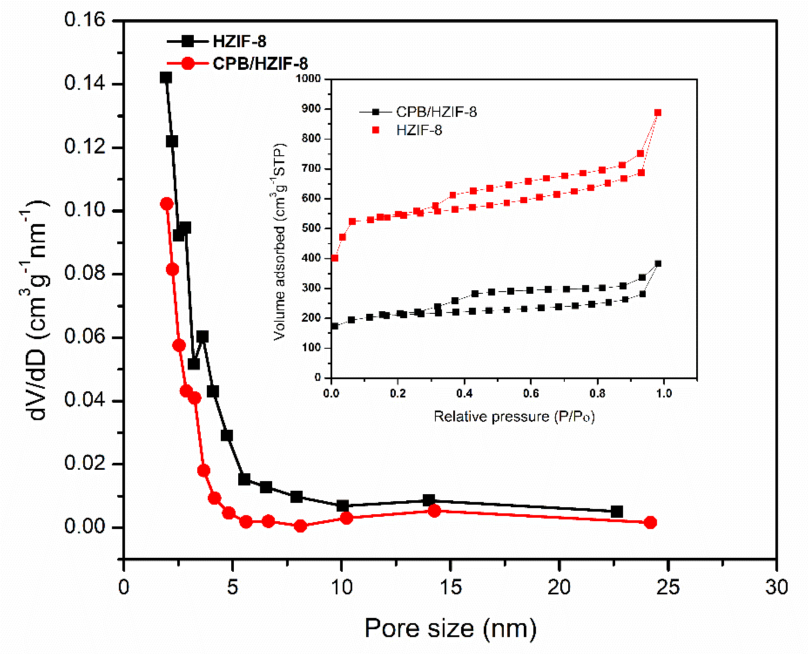

Figure 4.6: Pore size distributions and N_2 adsorption-desorption isotherms (inset) of HZIF-8 and $CsPbBr_3$/HZIF-8 (d).

Table 4.1. Parameters derived from BET isotherm of HZIF-8 MOF and $CsPbBr_3$/HZIF-8 MOF

Samples	**Surface area** ***(m^2g^{-1})*** ***(S_{BET})***	**External surface area, *(m^2g^{-1})*** ***(S_{meso})***	***S_{micro}*** ***(m^2g^{-1})***	**Pore Volume** ***(cm^3g^{-1})*** ***(V_{total})***
HZIF-8	2065.237	300.84	1764.39	0.707
$CsPbBr_3$/ HZIF-8	788.116	166.267	621.85	0.308

4.3.6. Photophysical properties

Figure 4.7b displays the UV-Vis spectra of HZIF-8 and $CsPbBr_3$/HZIF-8 where the MOF exhibits a weak absorption. In the presence of PeQDs, the absorption of HZIF-8 increases with an absorption peak at 509 nm. The PeQDs without the MOF matrix shows similar absorption behavior with the $CsPbBr_3$/HZIF-8 composite with the maxima starts at 512 nm. The composite shows an intense green emission with a peak centered at 510 nm with FWHM value of 25 nm on excitation with a light of 365 nm wavelength (Figure 4.7a). A small blue shift of 12 nm with a slight wider FWHM from the $CsPbBr_3$ without the HZIF-8 matrix indicates the confinement effect of the PeQDs due to size restriction of the PeQDs by the MOF matrix. The PLQY of CPB/HZIF-8 composite in toluene solution was calculated to be 45.5 % using fluorescein as the reference standard.

The time resolved PL decay dynamics of bare $CsPbBr_3$ and CPB/HZIF-8 composite were further studied in which the MOF embedded $CsPbBr_3$ shows slower decay kinetics than the bare $CsPbBr_3$ (Figure 4.7c). The increase in the life time of $CsPbBr_3$ is associated with the surface defect passivation of PeQDs by the MOF matrix. The decay parameters are summarized in Table 4.2. The formula used to calculate average life time is-

$$\tau_{avg} = (\sum A_i\tau_i^2) / \Sigma A_i\tau_i \quad , i = 1,2,3 \qquad (4.1)$$

where τ_i signifies parameters of lifetime decay and A_i is a constant termed as pre-exponential factors, τ_{avg} denotes the average lifetime [22].

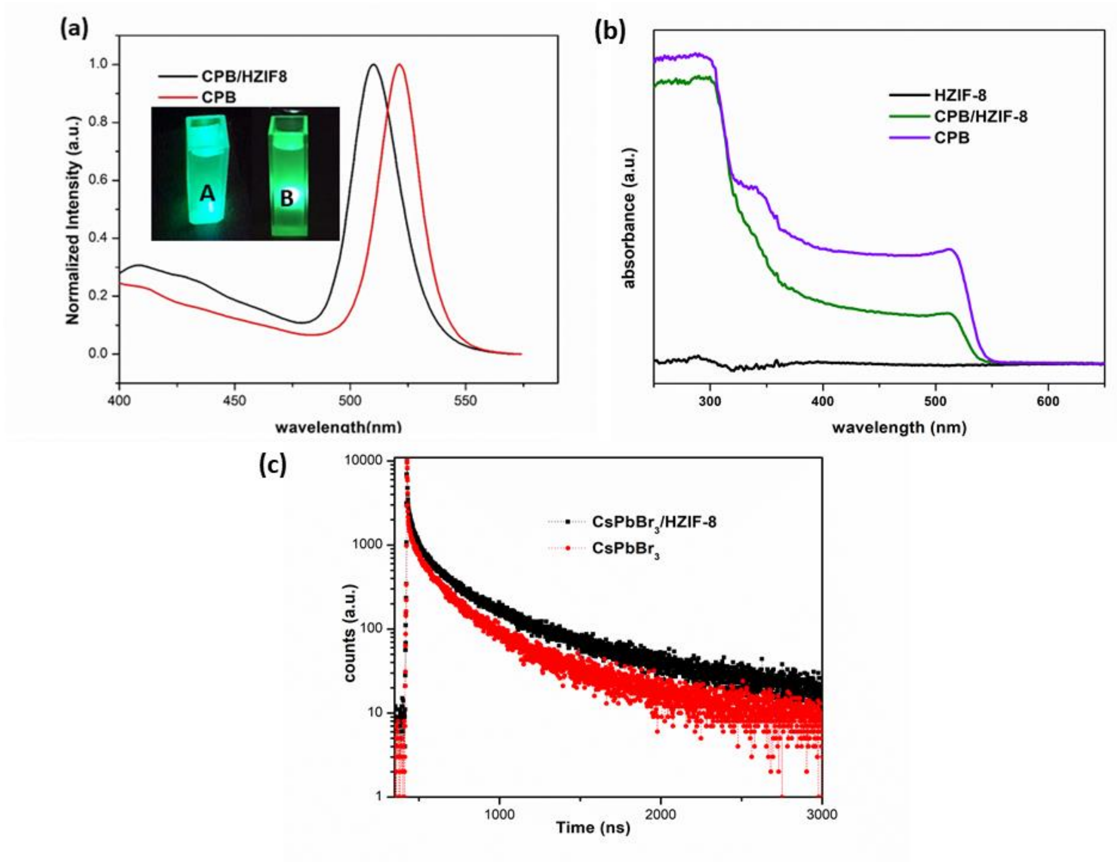

Figure 4.7: PL spectra of $CsPbBr_3$ (No MOF- Red) and $CsPbBr_3$/HZIF-8 (Black), inset: corresponding photographs of $CsPbBr_3$ (B) and $CsPbBr_3$/HZIF-8 (A) under 365 nm UV lamp (a), Absorption spectra of HZIF-8 (black), $CsPbBr_3$/HZIF-8 (green) and $CsPbBr_3$ (purple) (b), TRPL decay graphs of $CsPbBr_3$ (red) and $CsPbBr_3$/HZIF-8 (black) (c).

4.3.7. Stability test of $CsPbBr_3$/HZIF-8 composite

In general, due to the extra sensitive nature of $CsPbBr_3$ PeNCs, their applications in analytical field are limited. The HZIF-8 MOF matrix provides extra stability to the PeNCs, making it highly stable in ambient conditions. Figure 4.8a shows the stability of the composite powder against long term storage in open air conditions at room temperature (~ 70% humidity). The resulting powder retains its 95 % of luminescence intensity for about two months whereas the PL intensity of CPB PeNCs is practically quenched. Furthermore, the UV photo-stability of the $CsPbBr_3$/HZIF-8 composite was tested by being exposed to 365 nm UV light in an ambient atmosphere, with the PL intensity being checked at various intervals of exposure time. On exposure of 80 hours, the composite maintains 80 % of its initial PL intensity. The aqueous stability of the prepared $CsPbBr_3$/HZIF-8 composite was investigated by recording its PL after soaking the composite powder in an aqueous solution. The composite formed a well dispersed solution in water while maintaining its intense green emission. We checked the emission spectra of the water dispersed solution for a time period of 15 days (Figure 4.8c).

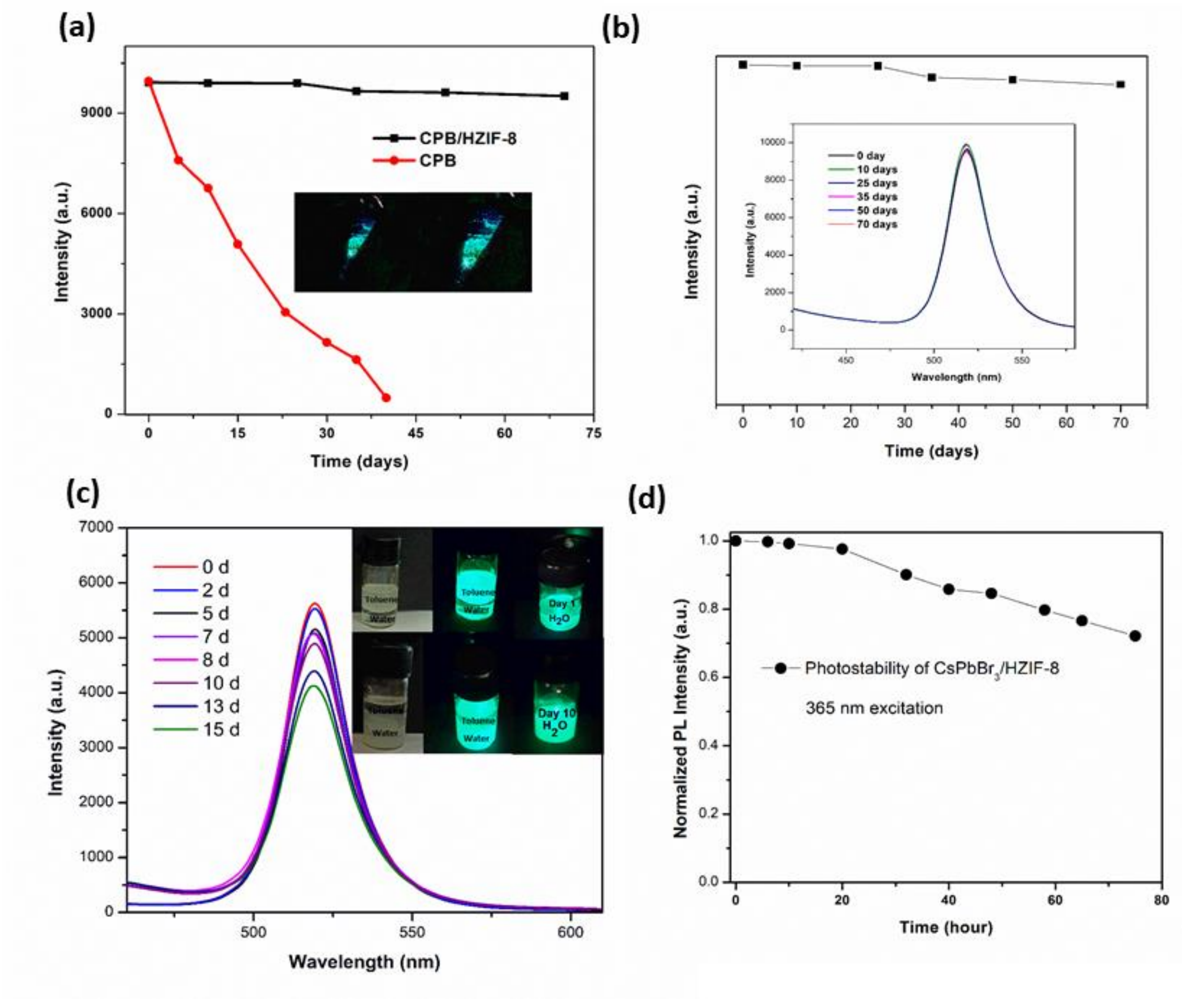

Figure 4.8: Storage test of $CsPbBr_3$/HZIF-8 (a, b), Intensity vs. time plot of bare $CsPbBr_3$ (red) and $CsPbBr_3$/HZIF-8 (black), inset: Photographs of $CsPbBr_3$/HZIF-8 powder in day 1 and day 60 under 365 nm UV light, (c) Emission spectra evolution of aqueous $CsPbBr_3$/HZIF-8 dispersion for 15 days and (d) UV Photo-stability test of the composite.

4.3.8. $CsPbBr_3$/HZIF-8 composite in chemical sensing application

As discussed above, the highly improved fluorescence properties of $CsPbBr_3$/HZIF-8 composite material enable them to utilize in optical sensing applications. Therefore, the potential use of the suggested material in the field of fluorescence chemo sensing was examined.

4.3.8.1. PL Quenching of the probe by Cu^{2+} metal ion: Figure 4.9a displays the PL response of $CsPbBr_3$/HZIF-8 with increasing concentration of Cu^{2+}. The intense green emission of $CsPbBr_3$/HZIF-8, centered at 510 nm was quenched with the addition of Cu^{2+} from 30 to 1500 nM concentration. Stern-Volmer relation (equation 2.5) was used to analyze the quenching behavior of the $CsPbBr_3$/HZIF-8 where the quenched ratio F_0/F and copper concentration are shown to be linearly correlated (Figure 4.9b) in the range of 30-1500 nM. The calibration curve was successfully fitted to the equation, Y = 0.0045 X + 0.695, with a correlation coefficient (R^2) of 0.9957. The quenching constant (K_{sv}) value was found to be 4.5×10^6 M^{-1}. The limit of detection (LOD) of Cu^{2+} was determined to be 4.66 nM using the relation 3σ/S, where S is slope of the linear calibration graph and σ represents standard deviation [23]. Thus, Cu^{2+} metal ion acted as an effective quencher for the designed sensor.

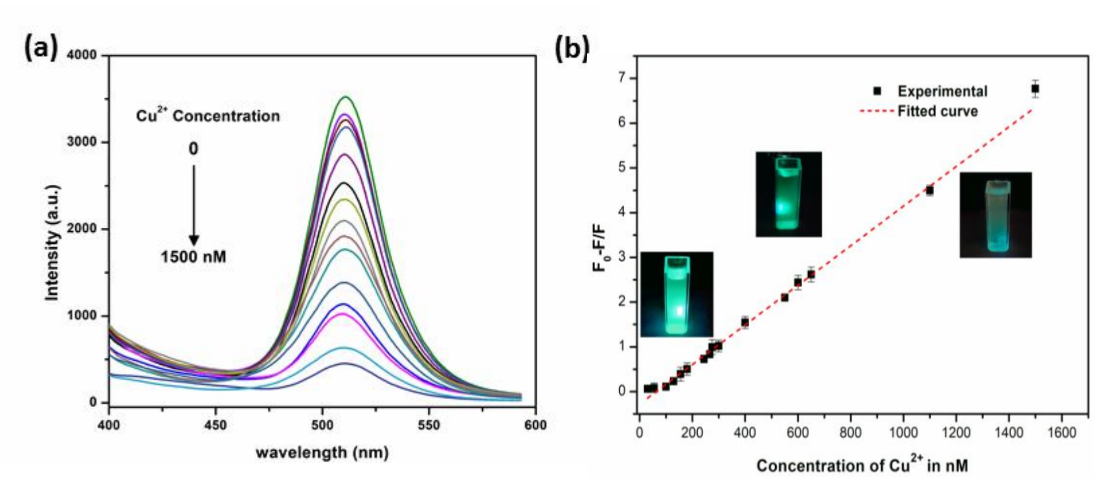

Figure 4.9: PL spectra of $CsPbBr_3$/HZIF-8 with various concentration of Cu^{2+} (a), Calibration graph versus concentration of Cu^{2+} metal ions (b).

4.3.8.2 Analytical performance for melamine sensing

As discussed above, the PL signal at 510 nm was quenched considerably in the presence of Cu^{2+} ion constructs a turn-off PL sensing system. When melamine is added to $CsPbBr_3$/HZIF-8-Cu^{2+}system under optimum experimental conditions, it could release the adsorbed copper ion from the surface of $CsPbBr_3$/HZIF-8, and eventually restore the quenched signal. In order to achieve the optimal and sensitive "off-on" response of $CsPbBr_3$/HZIF-8 probe for melamine detection, the influence of reaction time and pH value was studied (Figure 4.10a and b). The recovery of the PL signal begins within a minute and rises with time from 0 to 5 minutes, and reaches a maximum at 10 min. The system becomes steady after 10 minutes and has been tested for up to 30 minutes. Similarly, with the increasing pH from 4.5 to 6.5, the recovery increases and then decreases at higher pH. An incubation time of 10 minutes and a solution pH of 6.5 was used for further sensing experiments.

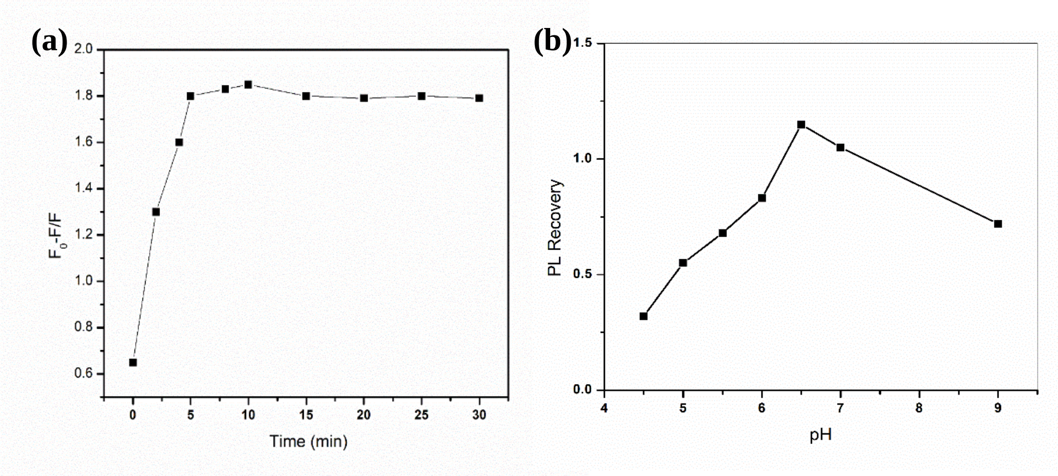

Figure 4.10: PL recovery of the $CsPbBr_3$/HZIF-8 with melamine addition for an incubation period of 30 min (a), effect of pH (b).

The addition of only melamine to the $CsPbBr_3$/HZIF-8 has negligible impact on the emission spectrum of the composite (Figure 4.11a). Figure 4.11b illustrates the fluorescence response of $CsPbBr_3$/HZIF-8-Cu^{2+}system with the increasing concentration of melamine from 0-500 nM. The correlation between the concentration of melamine and the PL recovery efficiency $(F_0 - F)/F$, is presented in Figure 4.11c. F_0 and F represent the PL intensity of the composite in presence and absence of melamine, respectively. It is possible to express the calibration curve as a linearly fitted equation $(F - F_0)/F_0$ = 0.0051 C + 0.0866 (R^2 = 0.9906). The LOD (3σ/s) for melamine detection was estimated to be 2.64 nM, which is equivalent to an even better than those described in the literature (Table 4.4).

4.3.8.3 Selectivity study: To determine the selectivity of the sensing system for the detection of melamine, the effect of some possible interfering substances including glycine (Gly), Cysteine (Cys), Glutamic acid (Glu), P-phenylenediamine (P-Phe), Serine (Ser), alanine (ala), Fructose, Glucose, vit. C were examined. Figure 4.11d shows the luminescence of the $CsPbBr_3$/HZIF-8-Cu composite is not significantly impacted by other substances except melamine with multifunctional heterocyclic system. The foregoing data imply that our sensor has an adequate selectivity.

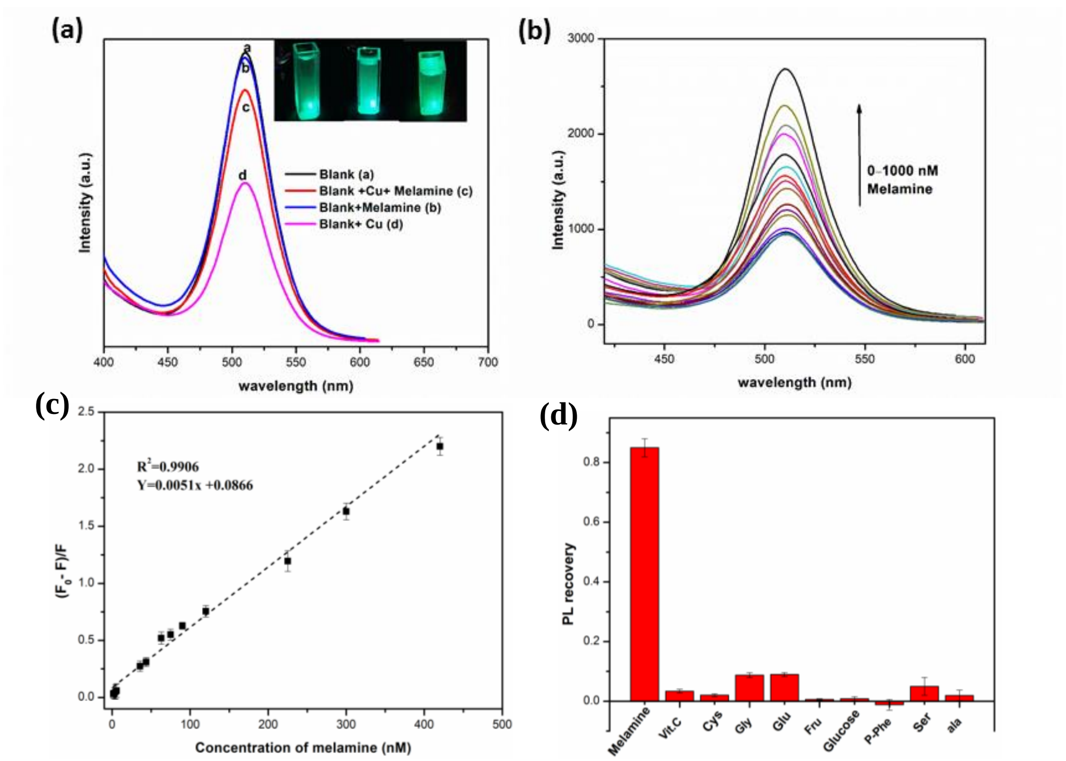

Figure 4.11: $CsPbBr_3$/HZIF-8 for melamine sensing- (a) inset: Photographs showing the recovery of green emission of $CsPbBr_3$/HZIF-8-Cu with melamine addition (left to right), (b) PL response of ($CsPbBr_3$/HZIF-8 + Cu) with the addition of different concentration of melamine, (c) Calibration curve, (d) Selectivity of the sensing probe with other biological molecules.

4.3.8.4 A plausible mechanism of sensing

The proposed sensor exhibited a quenching behavior with Cu^{2+} metal ions. When Cu^{2+} was adsorbed on the surface of $CsPbBr_3$/HZIF-8 composite, a coordination complex (-Br-Cu-N-MOF) can be formed due to the interaction between Br^- ion of $CsPbBr_3$ and Cu metal ion. In the FTIR spectra (Figure 4.12a) of the composite after Cu^{2+} addition, we have observed a distinct peak shifting of N-H stretching vibration indicating the formation of coordination complex. Also, the XPS spectra of Br of $CsPbBr_3$/HZIF-8 was positively shifted after interaction with Cu^{2+} ion (Figure 4.13 a), indicating the coordination between bromine of the perovskite and Cu metal ion. Thus, the interaction with Cu^{2+} might produce some new surface states or defect levels in the perovskite nanocrystals facilitating nonradiative pathways for electron/ hole recombination and finally quench the FL signal of $CsPbBr_3$ perovskite composite [24]. When melamine is added, there is a competitive binding interaction between perovskite and the melamine. Due to strong binding interaction of melamine with Cu, it removes the Cu ion from the surface of the composite, and finally recovers the PL. The interaction of melamine with Cu can be verified by the UV –vis absorption spectra presented in Figure 4.12b, where the presence of Cu significantly changes the absorption spectrum of melamine. The absorption peak of melamine at 202 nm shifts towards the right and the peak at about 234 nm disappears with the addition of Cu^{2+}. The interaction is further supported by the XPS spectra. The shift noticed in the XPS spectrum of Br after Cu metal ion addition was disappeared after melamine was added to the sensing probe confirms the aforesaid findings (Figure 4.13b).

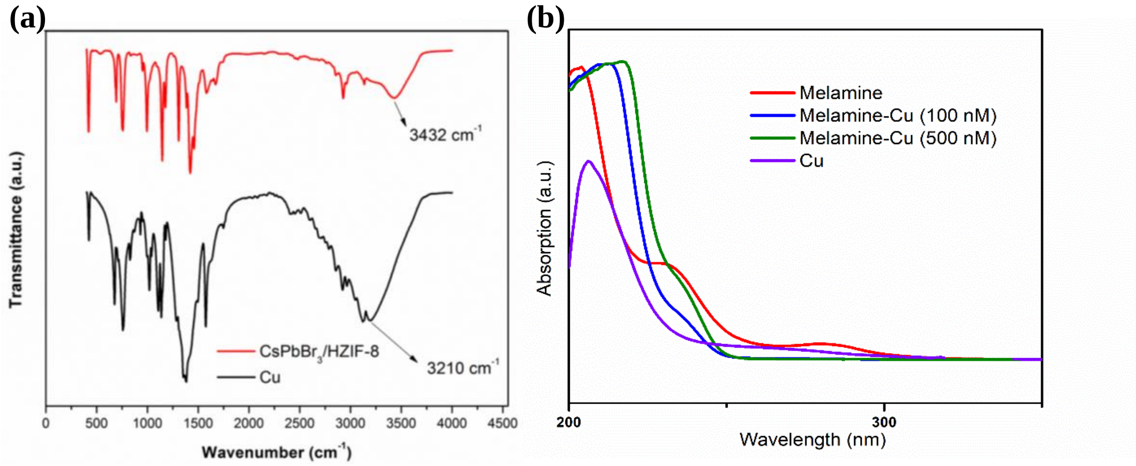

Figure 4.12: FTIR spectra of $CsPbBr_3$/HZIF-8 with copper metal ion (a), UV- vis absorption spectra of melamine (red), Cu^{2+} (purple), Cu-melamine (blue, green).

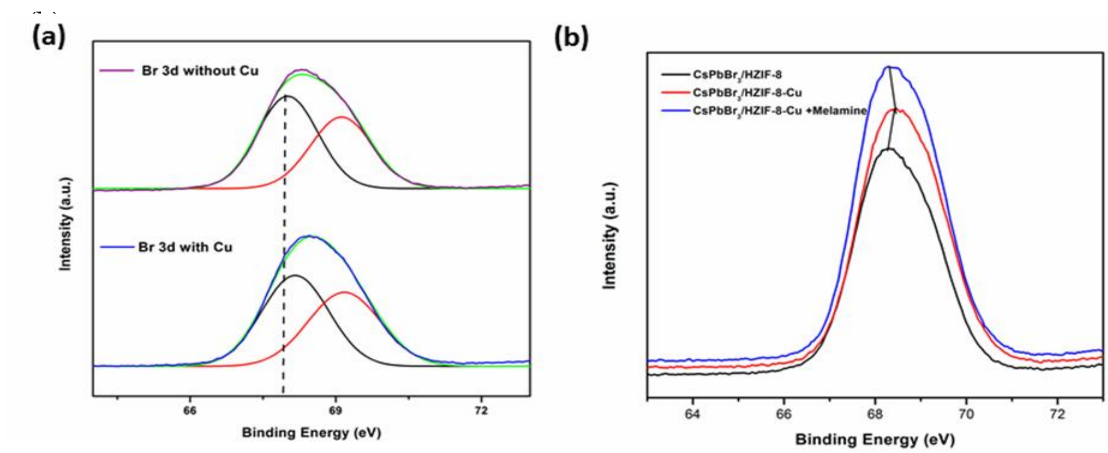

Figure 4.13: (a) High resolution XPS spectra of Br 3d with and without the addition of Cu^{2+} metal ion, (b) Comparison with the XPS spectra of Br after melamine addition to the $CsPbBr_3$/HZIF-8-Cu.

TRPL decay dynamics of $CsPbBr_3$/HZIF-8-Cu in presence of melamine is presented in Figure 4.14b. The melamine itself showed no significant change in the FL lifetime of the $CsPbBr_3$/HZIF-8. The reduced average lifetime of $CsPbBr_3$/HZIF-8-Cu was restored from 19.28 ns to 37.32 ns after the introduction of 250 nM melamine (Table 4.2) signifying the removal of non-radiative recombination pathways and further corresponding to the recovery of the quenched PL intensity of the designed sensing system.

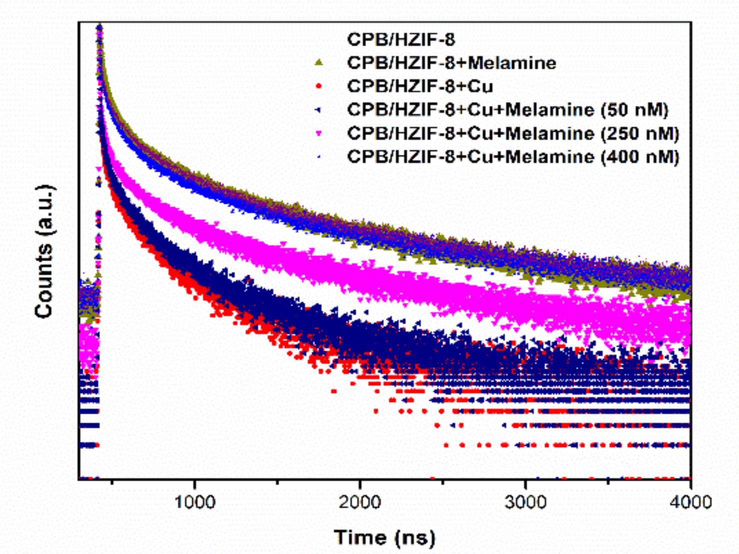

Figure 4.14: Fluorescence decay graph of $CsPbBr_3$/HZIF-8-Cu with various concentration of melamine.

Table 4.2. Summary of TRPL decay lifetimes result

Samples	τ_1 (ns)	τ_2 (ns)	τ_3 (ns)	τ_{avg} (ns)
$CsPbBr_3$/HZIF-8	13.37	26.75	53.51	40.13
$CsPbBr_3$	8.329	16.66	33.33	25.23
$CsPbBr_3$/HZIF-8 + Melamine	13.18	26.36	52.73	39.54
$CsPbBr_3$/HZIF-8 + Cu(160 nM)	6.42	12.84	25.72	19.29
$CsPbBr_3$/HZIF-8 + Cu + Melamine (50 nM)	7.38	14.77	29.54	22.15
$CsPbBr_3$/HZIF-8 + Cu + Melamine (250 nM)	12.43	24.88	49.77	37.32
$CsPbBr_3$/HZIF-8 + Cu + Melamine (400 nM)	13.13	26.50	52.50	39.45

4.3.8.5 Practical application of the sensor in milk samples

To know the practicability of the sensor, we further employ this switchable fluorescent nano sensor to detect melamine in milk samples (liquid raw milk and infant formula). The standard spiked recovery studies were utilized to assess the precision of our established probe. The melamine was spiked at various quantities in each sample, and the fluorescence signal was then assessed. The data presented in Table 4.3 showed the melamine recoveries in the spiked samples at three different concentrations from 94.7 % to 100.8 % with RSD (relative standard deviation) not exceeding 6.37%, signifying that the proposed fluorescent sensing platform is a reliable method for the detection of melamine in dairy products and has a good applicability.

Table 4.3. Summary of melamine detection in real samples

Sample	Spiked (nM)	Detected (nM)	Recovery %	RSD % (n=3)
Raw Milk	0	Not detected	–	–
	45	45.4	100.8	2.73
	85	80.5	94.7	6.37
	145	141.5	97.58	2.27
Infant formula	0	Not detected	–	–
	45	44.5	98.8	5.68
	85	85.2	100.2	5.37
	145	140.5	96.8	4.88

Table 4.4. Performance of $CsPbBr_3$/HZIF-8 MOF based fluorescent sensor and comparison with the previously reported literature for the detection of melamine

Fluorescent System	Performance/LOD (nM)	Linear range (M)	Response time	Ref
UiO-66-NH2@Ru	90 nM	0.27 to 110 μM	3min	[25]
PDA-GNPs-Ag	23 nM	0.1 to 40 μM	N/A	[26]
Graphene QDs	0.12 μM	0.15−20 μM	10 min	[27]
Rhodamine B-AuNPs	0.18 μg L^{-1}	5−1000 μg L^{-1}.	7 min	[28]
C-dot-AuNPs	36 nM	0.05 – 0.5 μM	5 min	[29]
N-CQDs-Fe	660 nM	2–290 μM	30 min	[30]
AuNCs	28.2 μM	100 μM to 8 mM	N/ A	[31]
SiCQDs	8.0 nM	50 – 500 nM	5 min	[32]
BDFC- AuNPs	3.0 nM	10 – 4000 nM	30 min	[33]
$CsPbBr_3$/HZIF-8	2.64 nM	3-500 nM	10 min	This work

4.4. Conclusion

- ✓ A stable and effective sensing platform was designed by incorporating $CsPbBr_3$ PeQDs into a hierarchically porous HZIF-8, using an easy in-situ (two-step) growth method.
- ✓ A uniform distribution of $CsPbBr_3$ PeQDs in the HZIF-8 MOF matrix was observed and the composite exhibited an intense green emission at 510 nm with a FWHM value of 25 nm.
- ✓ Good fluorescence intensity and great stability were maintained after the transition of the synthesized $CsPbBr_3$/HZIF-8 composites to the aqueous phase.
- ✓ Further, the designed sensor was utilized for the on-off-on detection of melamine. The Cu^{2+} analyte acted as an effective quencher that quenches the green emission of $CsPbBr_3$. The quenched emission of $CsPbBr_3$/HZIF-8 was restored by the

competitive adsorption of $Cu^{2+}$from the surface of the sensor by the functional amine group of melamine.

- ✓ The designed sensor was found to be very sensitive toward melamine detection, with a limit of detection value of around 2.64 nM.
- ✓ The sensor was used to find melamine in real samples with satisfactory recoveries.

4.5. References

[1] Li, L., Wu, G., Hong, T., Yin, Z., Sun, D., Abdel-Halim, E. S., and Zhu, J. J. Graphene quantum dots as fluorescence probes for turn-off sensing of melamine in the presence of Hg2+. *ACS applied materials & interfaces,* 6(4):2858-2864, 2014.

[2] Zhu, L., Gamez, G., Chen, H., Chingin, K., and Zenobi, R. Rapid detection of melamine in untreated milk and wheat gluten by ultrasound-assisted extractive electrospray ionization mass spectrometry (EESI-MS). *Chemical Communications*, (5):559-561, 2009.

[3] Lu, Q., Zhao, J., Xue, S., Yin, P., Zhang, Y., and Yao, S. A “turn-on” fluorescent sensor for ultrasensitive detection of melamine based on a new fluorescence probe and AuNPs. *Analyst*, 140(4):1155-1160, 2015.

[4] Venkatasami, G. and Sowa Jr, J. R. A rapid, acetonitrile-free, HPLC method for determination of melamine in infant formula. *Analytica Chimica Acta*, 665(2):227-230, 2010.

[5] Goscinny, S., Hanot, V., Halbardier, J. F., Michelet, J. Y., and Van Loco, J. Rapid analysis of melamine residue in milk, milk products, bakery goods and flour by ultra-performance liquid chromatography/tandem mass spectrometry: from food crisis to accreditation. *Food Control*, 22(2):226-230, 2011.

[6] Liao, C. W., Chen, Y. R., Chang, J. L., and Zen, J. M. Single-run electrochemical determination of melamine in dairy products and pet foods. *Journal of agricultural and food chemistry*, 59(18):9782-9787, 2011.

[7] Chen, W., Deng, H. H., Hong, L., Wu, Z. Q., Wang, S., Liu, A.L., Lin, X. H., and Xia, X. H. Bare gold nanoparticles as facile and sensitive colorimetric probe for melamine detection. *Analyst*, 137(22):5382-5386, 2012.

[8] Liu, J., Zhong, Y., Liu, J., Zhang, H., Xi, J., and Wang, J., An enzyme linked immunosorbent assay for the determination of cyromazine and melamine residues in animal muscle tissues. *Food Control*, 21(11):1482-1487, 2010.

[9] Chen, L. M. and Liu, Y. N. Surface-enhanced Raman detection of melamine on silver-nanoparticle-decorated silver/carbon nanospheres: effect of metal ions. *ACS applied materials & interfaces*, 3(8):3091-3096, 2011.

[10] Guo, L., Liu, Y., Kong, R., Chen, G., Wang, H., Wang, X., Xia, L., and Qu, F. Turn-on fluorescence detection of β-glucuronidase using RhB@ MOF-5 as an ultrasensitive nanoprobe. *Sensors and Actuators B: Chemical*, 295:1-6, 2019.

[11] Jalili, R., Khataee, A., Rashidi, M. R., and Luque, R. Dual-colored carbon dot encapsulated metal-organic framework for ratiometric detection of glutathione. *Sensors and Actuators B: Chemical*, 297:126775, 2019.

[12] Cuan, J., Zhang, D., Xing, W., Han, J., Zhou, H., and Zhou, Y. Confining CsPbX3 perovskites in a hierarchically porous MOF as efficient and stable phosphors for white LED. *Chemical Engineering Journal*, 425:131556, 2021.

[13] Ren, J., Li, T., Zhou, X., Dong, X., Shorokhov, A. V., Semenov, M. B., and Wang, Y. Encapsulating all-inorganic perovskite quantum dots into mesoporous metal organic frameworks with significantly enhanced stability for optoelectronic applications. *Chemical Engineering Journal*, 358:30-39, 2019.

[14] Mollick, S., Mandal, T. N., Jana, A., Fajal, S., Desai, A. V., and Ghosh, S. K. Ultrastable luminescent hybrid bromide perovskite@ MOF nanocomposites for the degradation of organic pollutants in water. *ACS Applied Nano Materials*, 2(3):1333-1340, 2019.

[15] Cha, J. H., Noh, K., Yin, W., Lee, Y., Park, Y., Ahn, T. K., Mayoral, A., Kim, J., Jung, D. Y., and Terasaki, O. Formation and encapsulation of all-inorganic lead halide perovskites at room temperature in metal–organic frameworks. *The Journal of Physical Chemistry Letters*, 10(9):2270-2277, 2019.

[16] Cao, Y., Zhou, Y., Lin, Y., and Zhu, J. J. Hierarchical metal–organic framework-confined CsPbBr3 quantum dots and aminated carbon dots: A new self-sustaining suprastructure for electrochemiluminescence bioanalysis. *Analytical Chemistry*, 93(3):1818-1825, 2020.

[17] Yao, T., Dong, G., Qian, S., Cui, Y., Chen, X., Tan, T., and Li, L. Persistent luminescence nanoparticles/hierarchical porous ZIF-8 nanohybrids for

autoluminescence-free detection of dopamine. *Sensors and Actuators B: Chemical*, 357:131470, 2022.

[18] Abdelhamid, H. N., Huang, Z., El-Zohry, A. M., Zheng, H., and Zou, X. A fast and scalable approach for synthesis of hierarchical porous zeolitic imidazolate frameworks and one-pot encapsulation of target molecules. *Inorganic chemistry*, 56(15):9139-9146, 2017.

[19] Tang, L., Mo, S., Liu, S. G., Ling, Y., Zhang, X. F., Li, N. B., and Luo, H. Q. A sensitive "Turn-On" fluorescent sensor for melamine based on FRET effect between polydopamine-glutathione nanoparticles and Ag nanoparticles. *Journal of agricultural and food chemistry*, 66(9):2174-2179, 2018.

[20] Zhang, Z., Luo, X., Wang, B., and Zhang, J. Electron transport improvement of perovskite solar cells via a ZIF-8-derived porous carbon skeleton. *ACS Applied Energy Materials*, *2*(4):2760-2768, 2019.

[21] Kong, Z. C., Liao, J. F., Dong, Y. J., Xu, Y. F., Chen, H. Y., Kuang, D. B., and Su, C. Y. Core@ shell CsPbBr3@ zeolitic imidazolate framework nanocomposite for efficient photocatalytic CO2 reduction. *ACS Energy Letters*, 3(11):2656-2662, 2018.

[22] Worku, M., Tian, Y., Zhou, C., Lin, H., Chaaban, M., Xu, L. J., He, Q., Beery, D., Zhou, Y., Lin, X., and Su, Y. F. Hollow metal halide perovskite nanocrystals with efficient blue emissions. *Science Advances*, 6(17):5961, 2020.

[23] Ding, N., Zhou, D., Pan, G., Xu, W., Chen, X., Li, D., Zhang, X., Zhu, J., Ji, Y., and Song, H. Europium-doped lead-free Cs3Bi2Br9 perovskite quantum dots and ultrasensitive Cu2+ detection. *ACS Sustainable Chemistry & Engineering*, 7(9):8397-8404, 2019.

[24] Sheng, X., Liu, Y., Wang, Y., Li, Y., Wang, X., Wang, X., Dai, Z., Bao, J., and Xu, X. Cesium lead halide perovskite quantum dots as a photoluminescence probe for metal ions. *Advanced Materials*, 29(37):1700150, 2017.

[25] Lin, C., Zhong, C., Song, Y., and Wang, L. Ratiometric fluorescence detection of melamine in milk by a zirconium-based metal-organic frameworks composite. *Microchemical Journal*, 162:105837, 2021.

[26] Tang, L., Mo, S., Liu, S. G., Ling, Y., Zhang, X. F., Li, N. B., and Luo, H. Q. A sensitive "Turn-On" fluorescent sensor for melamine based on FRET effect

between polydopamine-glutathione nanoparticles and Ag nanoparticles. *Journal of agricultural and food chemistry*, 66(9):2174-2179, 2018.

[27] Li, L., Wu, G., Hong, T., Yin, Z., Sun, D., Abdel-Halim, E. S., and Zhu, J. J. Graphene quantum dots as fluorescence probes for turn-off sensing of melamine in the presence of Hg2+. *ACS Applied Materials & Interfaces*, 6(4):2858-2864, 2014.

[28] Cao, X., Shen, F., Zhang, M., Guo, J., Luo, Y., Xu, J., and Sun, C. Highly sensitive detection of melamine based on fluorescence resonance energy transfer between rhodamine B and gold nanoparticles. *Dyes and Pigments*, 111:99-107, 2014.

[29] Dai, H., Shi, Y., Wang, Y., Sun, Y., Hu, J., Ni, P., and Li, Z. A carbon dot based biosensor for melamine detection by fluorescence resonance energy transfer. *Sensors and Actuators B: Chemical*, 202:201-208, 2014.

[30] Zhuang, Q., Li, L., Ding, Y., Zeng, H., and Wu, Y. Highly Luminescent Nitrogen-Doped Carbon Dots as "Turn-On" Fluorescence Probe for Selective Detection of Melamine. *ChemistrySelect*, 4(1):84-89, 2019.

[31] Kalaiyarasan, G., Anusuya, K., and Joseph, J. Melamine dependent fluorescence of glutathione protected gold nanoclusters and ratiometric quantification of melamine in commercial cow milk and infant formula. *Applied Surface Science*, 420:963-969, 2017.

[32] Qian, Z., Shan, X., Chai, L., Ma, J., Chen, J., and Feng, H. Si-doped carbon quantum dots: a facile and general preparation strategy, bioimaging application, and multifunctional sensor. *ACS applied materials & interfaces*, 6(9):6797-6805, 2014.

[33] Lu, Q., Zhao, J., Xue, S., Yin, P., Zhang, Y., and Yao, S. A "turn-on" fluorescent sensor for ultrasensitive detection of melamine based on a new fluorescence probe and AuNPs. *Analyst*, 140(4):1155-1160.